Research Square

Preprints are preliminary reports that have not undergone peer review.
They should not be considered conclusive, used to inform clinical practice,
or referenced by the media as validated information.

# Direct tsunami wavefield sensing on submarine telecom cables enables coastal wave height forecasting

**Yuqing Xie**
Institute of Geology and Geophysics(IGG), Chinese Academy of Sciences(CAS)
**Diane Rivet**
diane.rivet@geoazur.unice.fr
Observatoire de la Côte d'Azur, Université Côte d'Azur, CNRS, IRD, Géoazur https://orcid.org/0000-0003-4697-4460
**Anthony Sladen**
Observatoire de la Côte d'Azur, Université Côte d'Azur, CNRS, IRD, Geoazur
**Martijn van den Ende**
Observatoire de la Côte d'Azur, Université Côte d'Azur, CNRS, IRD, Geoazur https://orcid.org/0000-0002-0634-7078
**Marie Baillet**
Observatoire de la Côte d'Azur, Université Côte d'Azur, CNRS, IRD, Geoazur
**Alister Trabattoni**
Observatoire de la Côte d'Azur, Université Côte d'Azur, CNRS, IRD, Geoazur
**Jean-Paul Ampuero**
Institut de Recherche pour le Développement https://orcid.org/0000-0002-4827-7987
**Sergio Barrientos**
Centro Sismológico Nacional, Universidad de Chile, Santiago, Chile.

**Article**

**Keywords:**

**Posted Date:** October 21st, 2026

**DOI:** https://doi.org/10.21203/rs.3.rs-10971438/v1

**License:** This work is licensed under a Creative Commons Attribution 4.0 International License.
Read Full License

**Additional Declarations:** There is **NO** Competing Interest.

# Abstract

Detecting tsunamis in the open ocean before they reach the coast is critical for saving lives, yet open-ocean observations remain sparse and costly. Submarine telecommunication cables span many tsunami-prone regions and can be instrumented with distributed sensing, but their tsunami sensitivity remains uncertain. Here we report observations of the transoceanic tsunami generated by the Mw 8.8 Kamchatka earthquake on 29 July 2025, obtained through distributed acoustic sensing (DAS) on a 400-km telecommunication cable array offshore Chile. After suppressing background and instrumental noise, we recover coherent tsunami signals along hundreds of kilometres of cable despite maximum open-ocean amplitudes of only ~ 4 cm. The recovered signals agree with tsunami simulations, while revealing spatial variability in cable sensitivity. Converting DAS strain to water elevation empirically, we reconstruct the tsunami wavefield and predict coastal tide-gauge records where constrained by high-fidelity cable segments, providing 5 to 15 minutes of warning time before the tsunami arrives at the coast. These results demonstrate the viability of an end-to-end tsunami warning system based on existing submarine cables.


# Main

Tsunamis are among the most destructive natural hazards. The 2004 Indian Ocean tsunami and the 2011 Tohoku tsunami remain two of the deadliest natural disasters in modern history, claiming over 230,000 and 22,000 lives, respectively [1, 2, 3]. In both cases, the amplitudes of tsunamis far exceeded authorities' expectations, exposing critical gaps in monitoring and warning capabilities [4]. These tragedies marked a turning point, prompting global efforts to improve tsunami forecasting and early warning systems. Earthquake observations provide rapid source information, but direct tsunami observations are needed to unequivocally constrain the evolving tsunami wavefield and to forecast coastal impact. This is especially true considering that tsunami hazards cannot be always reliably inferred from earthquake source parameters alone, and that some are caused by non-earthquake sources including submarine landslides and volcanic activity.

Substantial efforts have been made to expand direct offshore tsunami observations, most comprehensively through dense cabled pressure-sensor networks such as S-net and DONET/DONET2 in Japan [5, 6]. However, the high cost of such dedicated infrastructure precludes widespread deployment, leaving most of the world reliant on sparse open-ocean DART buoys [7] and large areas of the ocean without direct observations. Moreover, remote buoy outages remain an operational challenge [8]; for instance, four of 14 DART buoys examined in a 2016 network assessment were inoperative at the time of the study, potentially degrading tsunami-forecasting capability and requiring timely repair [9]. Without affordable and dependable monitoring solutions, many high-risk tsunami zones remain completely unequipped. Regions like the Makran Subduction Zone (Persian Gulf) are prime examples: despite significant tsunami hazards, their long or uncertain return periods make it difficult to justify implementing full warning infrastructure.

Submarine telecommunication cables instrumented with distributed acoustic sensing (DAS) provide a potential pathway to overcome these limitations by transforming existing seafloor infrastructure into large-scale offshore observation networks [10, 11 12]. Extending nearly 1.5 million km globally, these cables offer unprecedented spatial coverage without deploying new instruments offshore. By analysing changes in backscattered light, DAS converts optical fibres into dense arrays of longitudinal-strain sensors over thousands of kilometres [14]. The mechanisms by which a cable longitudinal strain can sense tsunamis have been quantified in principle [13]. However, tsunami observations by submarine DAS remain limited; in particular, direct, open-ocean observations of a tsunami wavefield are lacking, which is a crucial gap because resolving the wavefield in space and time is the only viable path towards forecasting coastal wave heights. Previous studies have detected tsunami-related signals [15–17], including from non-tectonic sources [18], but either through indirect inference [16], without resolving the tsunami wavefield [15, 17], or at much shorter periods than those of tectonic tsunamis [18]. A key question remains: can dense and continuous measurements, despite strong noise and spatially variable cable responses, resolve tsunami wavefields with sufficient fidelity to monitor tsunami evolution and forecast coastal wave heights?

## Direct observation of the tsunami wavefield

Here we report direct DAS observations of the 2025 Mw 8.8 Kamchatka tsunami on a 400-km-long submarine telecommunications cable array offshore central Chile. From nearly 26,000 sensing channels, we recover a coherent tsunami-induced wavefield over hundreds of kilometres of seafloor cables despite its small open-ocean amplitude and strong instrumental and ambient noise. We use these observations to demonstrate that submarine telecom cables are sufficiently sensitive to tsunami-induced deformation, allowing for the reliable forecasting of coastal impact and enabling DAS-based tsunami early warning.

The 2025 Mw 8.8 Kamchatka earthquake generated a transoceanic tsunami that was recorded by the ABYSS submarine DAS observatory offshore central Chile (Fig. 1) [19], providing a unique dataset for observing tsunami propagation along submarine telecommunications cables and assessing their potential for tsunami monitoring and forecasting. Operating since 30 September 2023, the observatory uses three sections of an existing submarine telecommunication cable network operated by GTD, with a total sensing range of ~ 400 km and 26,664 sensing channels. Three long-range DAS interrogators (ASN OptoDAS), located in the coastal cities of La Serena and Concón, continuously sensed three cable segments with 15 m spatial sampling and 62.5 Hz (CCN.N and SER.S) and 100 Hz sampling frequency (SER.N). The observatory offers a real-time data interface through SeedLink and ZeroMQ protocols [20], which have already been used to test earthquake early-warning prototypes [21, 22]. Thus, these real-time transmission capabilities, together with the embedded computing resources, already lay the required foundations for a tsunami warning system based on submarine telecom cables.

Simulations constrained by eight DART observations predict that the far-field tsunami reaching Chile had a root-mean-square (RMS) amplitude of only ~ 4 cm (Fig. 2). In the raw DAS data, before denoising, no coherent tsunami signal was distinguishable from the dominant instrumental noise within the predicted

arrival window. To extract the tsunami signals, it was crucial to reduce the common-mode instrumental noise. We estimated this noise in two steps. First, we applied a preliminary cable-wide common-mode correction to identify cable segments that are weakly sensitive to tsunami signals. We then used the spatial median of the data in these reference segments as an estimate of the common-mode noise, and removed it from the original data (Methods). We further applied temporal filtering in the expected range of tsunami periods (between 300 and 2000 s) and applied spatial filtering with a 2400-m sliding median window to exploit the long-wavelength coherence of tsunami waves along the cable, thereby reducing shorter-wavelength internal-wave contamination and local incoherent noise (Methods). This processing transforms the dense DAS array from a collection of noisy individual channels into a coherent line observation of the tsunami wavefield.

Despite large instrumental and environmental noise, we recovered coherent DAS signals in the tsunami period band (~ 1,000 s) along all three cable sections around the expected tsunami arrival time. Nearby tide-gauge records also show consistent arrival times and dominant periods when compared with DAS segments at similar latitudes (Fig. 1d).

The recovered tsunami response is spatially heterogeneous along the cable (Fig. S1), with local amplitude variations exceeding two orders of magnitude over distances much shorter than the tsunami wavelength. The strongest response occurs around 100 km on the SER.S cable (Fig. 1b). Such short-wavelength variability is unlikely to reflect the tsunami wavefield itself, and instead indicates a spatially variable transfer function between water pressure and cable strain. This transfer function may depend on cable burial, cable-seafloor coupling and seafloor topography, although these contributions cannot be uniquely separated with the present dataset. This spatially variable response represents a major challenge for converting DAS strain measurements into quantitative estimates of tsunami wave elevation.

# Sea-level change from DAS seafloor observation

To convert the observed DAS strain into sea-surface elevation, we first consider existing mechanical models. Tsunami pressure perturbations can generate cable strain through two main mechanisms, seafloor compliance and the Poisson effect of the cable. Both induce a first-order linear relation between pressure and DAS strain [13], leading to a strain-to-water-elevation conversion coefficient of $1.10^6$ to $1.10^7$ m/strain and $1.10^6$ to $5.10^6$ m/strain, respectively, for typical crustal and cable material properties. A recent submarine-cable tsunami observation also found DAS strain energy to scale approximately with nearby ocean-bottom pressure records, with a coefficient of order $10^7$-$10^8$ m/strain RMS in the 50–100 second period band [16]. However, neither a single proportionality coefficient nor the present mechanical models can reproduce the large channel-to-channel variations observed along the ABYSS cable. The relative contributions of compliance and Poisson effects, their possible superposition, and their dependence on poorly known cable-site conditions remain too uncertain for a purely physics-based strain-to-water-elevation conversion.

We therefore adopt an empirical approach and estimate channel-dependent conversion coefficients by matching observed DAS strain-rate amplitudes to simulated water-elevation-rate amplitudes at the corresponding cable locations (Methods, Fig. S2). For a linear strain–water-level relationship, the same proportionality applies to their time derivatives; the converted water-elevation-rate waveforms are later integrated to obtain water elevation for tsunami forecasting. We constrain the reference tsunami model with three nearest DART observations, and validate it by five DART stations, including one station located approximately 200 km from the cable system (Methods, Fig. S3 and S4). The obtained coefficients for most cable segments range from $1\times10^7$ m/strain to $5\times10^7$ m/strain, in line with theoretical estimates and previously reported observations [16, 23, 24, 25]. After conversion, the DAS-derived waveforms are expressed in water-elevation-rate and show a more uniform amplitude pattern (Fig. 2b). The converted DAS records also reproduce the main spatial structure, arrival sequence and dominant periods predicted by the reference simulation (Fig. 2c,d,e). This first-order calibration allows us to evaluate the potential of calibrated DAS observations for tsunami wavefield reconstruction and forecasting.

## Tsunami wavefield reconstruction and forecasting

To exploit continuous cable observations for tsunami forecasting, we develop a wavefield-reconstruction method. In this approach, tsunami signals recorded along the cable are injected at their corresponding positions in a forward tsunami simulation (Methods, Supplementary Text S1). Synthetic tests indicate that continuous DAS signals contain sufficient information to reconstruct the evolving tsunami wavefield and update coastal tsunami forecasts (Fig. 3b). Reliable estimates of the first major tsunami peak can be obtained 5–15 min prior to it reaching the coast (Fig. 3f, Supplementary Fig. S5, Text S2), depending on cable and coastal geometry. Coastal segments that are well constrained by nearby continuous cable observations show accurate arrival times and amplitudes, whereas segments located in coverage gaps show delayed convergence or larger amplitude errors.

We further test whether the observed DAS records can be used for wavefield reconstruction and coastal tsunami forecasting. The empirically converted cable waveforms were further spatially filtered, temporally integrated and used in the reconstruction framework, with all channels included except those previously identified as anomalously noisy by the automated RMS-based quality-control procedure (Methods). For the high signal-quality CCN.N cable segment, the reconstructed wavefield reproduces well the main tide-gauge waveforms, in terms of arrival times and amplitudes (Fig. 3e, Table S1). The largest timing offset occurs at Quintero, where the mismatch is mainly attributable to limited bathymetric resolution near the coast (Fig. S6).

This experiment provides a direct benchmark linking the observed cable records to coastal tsunami predictions. It supports three inter-related conclusions: that the dominant coherent component of the recovered DAS signals is directly tsunami-induced, that empirical strain-to-water-elevation conversion is accurate, and that the cable signal-to-noise ratio is sufficient for forecasting purposes in favourable segments. It also highlights a key advantage of dense DAS observations: coherent tsunami energy is

reinforced during wavefield propagation toward the coast, whereas incoherent instrumental and local oceanographic noise is naturally suppressed. Thus, this reconstruction based solely on DAS recordings provides a direct end-to-end demonstration that, in favourable high-quality segments, observed cable signals can be converted into coastal waveform constraints for real-time tsunami forecasting.

The empirical channel-dependent coefficients derived above provide a first-order empirical calibration for converting DAS strain into tsunami water-elevation estimates (Fig. S2). Once established, such coefficients could be applied a priori to future events, enabling real-time conversion without event-specific calibration, provided that the cable response remains sufficiently stable within the tsunami frequency band. More accurate operational conversion, however, will require validation with independent datasets and may also need transfer functions that depend on both the angle of incidence [13, 34] and frequency[16]. This empirical strategy is physically plausible because theoretical models predict a linear relationship between pressure forcing and cable strain [13], and observations from submarine cables support such behaviour [16, 24]. Combined with wavefield-reconstruction methods such as those presented here, calibrated DAS measurements could turn submarine telecommunications cables into a new operational paradigm for tsunami early-warning systems.

Overall, the transoceanic tsunami generated by the 2025 Mw 8.8 Kamchatka earthquake was continuously recorded along a 400-km submarine telecommunications cable array offshore Chile. Despite open-ocean tsunami amplitudes of only a few centimetres, coherent signals were recovered across nearly 26,000 sensing channels, demonstrating that the dense geometry of submarine DAS can compensate for noisy individual measurements by exploiting spatial coherence along the cable. These observations further reveal pronounced spatial variability in tsunami sensitivity, highlighting the role of local cable-environment interactions in shaping DAS responses to oceanic signals.

Our reconstruction experiments demonstrate the value of dense offshore observations for constraining tsunami propagation and providing actionable lead times for coastal hazard assessment. Synthetic benchmarks show that continuous cable records contain sufficient information to track the evolving tsunami wavefield and provide forecast lead times of several to tens of minutes, depending on coastal location and cable geometry. The recovered wavefield constraints support high spatial resolution and can resolve large waves arriving after the first tsunami wave, which has the potential to enhance the specificity and completeness of tsunami warnings [26]. Crucially, after empirical conversion from DAS strain to water elevation, the observed cable records reproduce the main tide-gauge waveform shapes despite the low signal-to-noise ratio of individual channels for this ~ 4 cm open-ocean tsunami. Beyond this far-field demonstration, future studies will need to address local tsunami scenarios. Near-field earthquake tsunamis may provide stronger signals, potentially yielding much higher-SNR tsunami wavefield observations, but introduce challenges such as seismic-wave contamination, missing information of seafloor deformation and DAS amplitude saturation.

Ongoing developments in DAS technology, including extended sensing range and improved long-period stability, are expected to further enhance the capability of submarine fibre networks. Combined with the

extensive global footprint of existing telecommunications infrastructure, these results show that submarine cables can provide a scalable and cost-effective complement to existing tsunami monitoring systems in vulnerable coastal regions, including those with long tsunami recurrence intervals.

## Methods

# Denoising

We converted the offshore Chile DAS phase-rate-gradient records in rad $m^{-1}s^{-1}$ to strain rate using the instrument sensitivity factor of $1.07 \times 10^{-7}$ strain per (rad $m^{-1}$). Because the continuous dataset was too large to process as one file, data was downloaded in one-hour blocks, low-pass filtered with a 20 s cutoff period, decimated from 62.5 Hz to an 8 s sampling interval, and then merged. We used a single-pass causal Butterworth filter because applying a zero-phase forward–backward filter to independent hourly blocks would distort amplitudes near block edges and introduce discontinuities after merging. We used the Xdas Python framework [27] for DAS data handling and processing.

The instrumental noise (strain rate ~ $1 \times 10^{-9}$ strain.s-1) dominates the original data and is largely common across all sensors within each cable. As a first common-mode correction step, we subtracted the cable-wide median at each time step from the decimated data. After this initial subtraction, we calculated the RMS amplitude of each channel over the complete 36 h interval from 00:00 UTC on 30 July to 12:00 UTC on 31 July 2025. We classified channels as anomalously noisy when their RMS exceeded the median channel RMS by more than 1.5 scaled median absolute deviations. Channels exceeding this threshold were muted in the processed DAS images and excluded from RMS-amplitude profile interpretation, rather than treated as physical zero-amplitude measurements. The cable-wide median would also contain signals with wavelengths of the same order as the cable lengths, including potential tsunami signals. We therefore identified cable segments with the lowest amplitudes in the tsunami frequency band after the initial common-mode removal step (Fig. S1), which likely mainly recorded instrumental noise. We then re-calculated the spatial median of the original decimated data exclusively over these reference segments to obtain a refined estimate of the common-mode noise. We subtracted this estimate from the original decimated data to produce the final common-mode-corrected dataset.

Then, we time filtered the DAS records in the tsunami period band between 300 and 2000 s using a zero-phase forward–backward filter. We additionally applied a spatial median filter with a 2400 m window along the cable. This spatial window is much shorter than the expected tsunami wavelength but long enough to reduce channel-scale fluctuations and shorter-wavelength internal-waves. We used the spatially smoothed version in Figs. 1 and 2, showing the continuity of the tsunami signal along the cable.

## Synthetic tsunami waves

We generated synthetic tsunami wavefields as a reference for comparison with the DAS observations, empirical DAS-to-water-level calibration, and validation of the wavefield-reconstruction framework. Given the spatial extent of the earthquake rupture, we derived an extended source model constrained by the three nearest DART buoys (21415, 21416 and 21419) well-distributed around the source on the Pacific side (Fig. S3). We inverted the slip using a non-negative least-squares scheme on a discretized 6×2 fault plane (strike = 198°, dip = 15°, each panel 72x36 km, rigidity = 30 GPa) compatible with the GCMT focal mechanism. We computed tsunami propagation using a non-linear shallow water wave approximation model [28] with the long-wave dispersion taken into account a posteriori on the tsunami wave height at the different DAS sensor positions [29]. We performed the simulations on a 2-minute bathymetry grid covering the Pacific basin (ETOPOv2 [30]), with model parameters and boundary conditions following standard configurations. We compared the resulting model with tsunami waveforms at selected offshore DART stations in the Pacific (Fig. S4) to confirm the fidelity of the reconstructed tsunami wavefield, at least for stations in the deep ocean. The DART station along the Peruvian coast (32402), north of the DAS-monitored cables, is well predicted both in phase and amplitude for at least the first 4-hours of tsunami propagation.

# Reconstruction method

We developed a forward wavefield-reconstruction framework in which we impose water-level time series along a submarine cable as an internal, time-varying boundary condition in a tsunami forward propagation model.

We represented the input using 520 reconstruction stations distributed along the fibre, with one reconstruction station selected for every 50 original DAS channels. We linearly interpolated the synthetic or observation-derived waveforms along the cable to 1 s sampling interval. We performed the forward simulation using the parallel COMCOT model, pCOMCOT [31, 32], with bathymetry from the GEBCO 2024 Grid at 15 arcsec resolution [33], linear shallow-water equations without numerical-dispersion correction, and a 1 s time step. The model domain extended from 81.5°W to 70.5°W and from 41.5°S to 21.0°S. Its outer computational boundaries were treated as reflective wall boundaries in pCOMCOT; we enlarged the domain to delay artificial boundary reflections beyond the 5000 s simulation window. At each update time, we imposed the synthetic or observation-derived water elevation from each station onto model grid cells within 5 km of that station, creating a continuous line of localized water-elevation constraints along the cable. If multiple stations constrained the same grid cell, we updated the cell value sequentially from south to north. Thus, the cable input acts as a record-driven internal boundary condition for a forward simulation, rather than as an inversion or data-assimilation constraint.

The resulting forward simulation provides tsunami wavefields from which we extracted water-elevation waveforms at target locations, including coastal validation points and tide gauges. As additional cable records become available, we update the boundary condition and continue forward propagation from the updated wavefield to extend coastal predictions in time.

We first evaluated the method using an idealized benchmark (Text S1), where we sampled simulated tsunami water-elevation waveforms from the reference Kamchatka simulation along the ABYSS cable and at virtual validation stations along the coast, ensuring that we know both the offshore cable input and the target coastal waveforms. Then we applied it to the observation-derived tsunami waveforms (Text S3).

## DAS-to-water-level conversion

For the observation-driven reconstruction, we first converted DAS strain-rate records to water-elevation-rate-equivalent waveforms using empirical, channel-dependent RMS scaling factors, following the linear strain–water-level relationship described above. For each DAS channel, we calculated the RMS amplitude of both the processed observed strain-rate waveform and the collocated synthetic water-elevation-rate waveform during the tsunami window from 20:00 to 23:00 UTC on 30 July 2025. We defined the channel-specific calibration coefficient shown in Fig. S2 as the synthetic water-elevation-rate RMS divided by the observed DAS strain-rate RMS. Valid calibration points spanned 16.6–100.0 km for SER.N, 16.0-136.1 km for SER.S, and 17.5-119.8 km for CCN.N, with internal gaps where DAS records were unavailable or had been set to zero after being identified as anomalously noisy during preprocessing. We linearly interpolated the calibration coefficients across these internal gaps and retained the nearest valid endpoint value outside these distance bounds. We then multiplied each processed DAS record by the resulting coefficient.

We then processed the converted waveforms jointly across the three cable segments using a two-dimensional geographic median filter with an 8-km radius(Fig. S8, S9). Channels located on land were excluded from the spatial-median calculation. At each time sample, we excluded from the median calculation the channels previously identified as anomalously noisy by the automated RMS-based quality-control procedure and subsequently set to zero. Of the remaining channel values, we discarded the 40% with the smallest absolute amplitudes and calculated the median of the retained values. Near the common SER.N–SER.S landing, the median could include valid offshore channels from either segment within the 8-km radius. Filtered values were extrapolated shoreward by no more than 8 km from the first valid offshore sensor; locations farther landward remained unfilled. We used this strong spatial filtering to emphasize coherent tsunami energy and enhance the spatial continuity of the reconstruction input, at the expense of native DAS spatial resolution. As a diagnostic check, we repeated the RMS calculation over a pre-arrival noise window from 00:00 to 19:00 UTC on 30 July 2025. We compared converted tsunami window and noise window RMS profiles, before and after the spatial filter, with the synthetic signal RMS profile, as shown in Figure S9.

We then interpolated the filtered water-elevation-rate-equivalent records onto 520 reconstruction stations using the four nearest DAS channels with inverse-distance-squared weights, resampled to 1 s, and integrated in time to water elevation. We demeaned and linearly detrended each integrated station waveform. We assigned zero weight to stations with RMS values below the 0.01 m threshold, so that they did not impose constraints on the reconstructed wavefield.

# Declarations

## ADDITIONAL SECTIONS

### Data Availability Statement

The processed DAS data products used in this study, including the 8-s sampled, zero-phase-filtered DAS waveforms, synthetic tsunami waveforms, conversion inputs, and the observation-based PCOMCOT reconstruction-input package, are openly available through Zenodo at https://doi.org/10.5281/zenodo.22283980. High-resolution raw DAS recordings are available from the corresponding authors upon reasonable request. Deep-ocean tsunami observations, where used, are available from the NOAA National Data Buoy Center DART archive (NDBC DART data access); Coastal water-level observations were obtained from the Chilean Hydrographic and Oceanographic Service (SHOA/CENDHOC; CENDHOC portal).

### Code Availability Statement

The Python/Jupyter workflows used in this study are openly available at https://github.com/xieyqgeo/tsunami-abyss-reconstruction, and the version used here is archived on Zenodo (DOI: https://doi.org/10.5281/zenodo.22283980). The repository covers (1) DAS preprocessing, (2) conversion of DAS strain rate to water-elevation rate and preparation of the reconstruction inputs, and (3) preparation and post-processing of the observation-driven reconstruction with PCOMCOT. The computational environment is specified in environment.yml. The workflows use NumPy, SciPy, pandas, Matplotlib, xarray, xdas and Jupyter.

The reconstruction itself was run with a legacy PCOMCOT F3.0 time-reversal branch, which an author of An and Meng (2017) provided privately. This branch is distinct from the public PCOMCOT 2.1 repository and is not redistributed here because of upstream restrictions on its release. The reconstruction-input package in the repository is compatible with this branch. The branch's key extension, described in An and Meng (2017) and summarized in the Methods, allows multiple spatially distributed point forcings with independent time-varying waveforms, and the present reconstruction relies on this capability.

### Acknowledgments

### Funding

This work was funded by the European Research Council (ERC) under the European Union's Horizon Europe programme (grant agreements 101041092—ABYSS and 101058129—DT-GEO). J.P.A. also received support from the French government through the UCAJEDI Investments in the Future programme (ANR-15-IDEX-01) managed by the National Research Agency (ANR).

### Author information

### Present address

Yuqing Xie

Institute of Geology and Geophysics, Chinese Academy of Sciences, Beijing, China

**Authors and Affiliations**

Géoazur, Université Côte d'Azur, CNRS, IRD, Observatoire de la Côte d'Azur, Valbonne, France

Yuqing Xie, Diane Rivet, Anthony Sladen, Martijn van den Ende, Alister Trabattoni, Marie Baillet, Jean-Paul Ampuero

National Seismological Center, University of Chile, Santiago, Chile

Sergio Barrientos

**Author Contributions**

**Conceptualization:**
Diane Rivet, Jean-Paul Ampuero, Anthony Sladen, Yuqing Xie

**Methodology:**
Diane Rivet, Yuqing Xie, Anthony Sladen, Jean-Paul Ampuero, Martijn van den Ende, Alister Trabattoni

**Investigation:**
Yuqing Xie, Diane Rivet, Anthony Sladen

**Formal analysis:**
Diane Rivet, Yuqing Xie, Anthony Sladen

**Software:**
Yuqing Xie, Diane Rivet, Martijn van den Ende

**Validation:**
Yuqing Xie, Diane Rivet, Anthony Sladen

**Visualization:**
Yuqing Xie, Diane Rivet

**Resources:**
Diane Rivet, Marie Baillet, Sergio Barrientos

**Funding acquisition:**
Diane Rivet

**Project administration:**
Diane Rivet

**Supervision:**
Diane Rivet, Jean-Paul Ampuero, Anthony Sladen

**Writing – original draft:**
Yuqing Xie

**Writing – review & editing:**
Yuqing Xie, Diane Rivet, Jean-Paul Ampuero, Anthony Sladen, Martijn van den Ende, Alister Trabattoni, Marie Baillet, Sergio Barrientos

**Ethics declarations**

**Competing Interests**

The authors declare no competing interests.

# References


1. Lay T, Kanamori H, Ammon CJ, Nettles M, Ward SN, Aster RC, Sipkin S (2005) The great Sumatra-Andaman earthquake of 26 december 2004. Science 308(5725):1127–1133
2. Uchida N, Bürgmann R (2020) A decade of lessons learned from the 2011 Tohoku–Oki earthquake. Rev. Geophys. 59, eRG000713 (2021)
3. Mori, N., Satake, K., Cox, D., Goda, K., Catalan, P. A., Ho, T. C., … Wilson, R.(2022). Giant tsunami monitoring, early warning and hazard assessment. Nature Reviews Earth & Environment, 3(9), 557–572
4. Mori N, Takahashi T, Yasuda T, Yanagisawa H (2011) Survey of 2011 Tohoku earthquake tsunami inundation and run-up. Geophysical research letters, 38(7)
5. Meinig C, Stalin SE, Nakamura AI, Milburn HB (2005) Real-time deep-ocean tsunami measuring, monitoring, and reporting system: The NOAA DART II description and disclosure. NOAA Pac Mar Environ Lab (PMEL), 1–15
6. Mochizuki M et al S-net project: performance of a large-scale seafloor observation network for preventing and reducing seismic and tsunami disasters. In OCEANS 2018-MTS/IEEE Kobe Techno-Oceans 1–4 (IEEE, 2018); https://ieeexplore.ieee.org/abstract/document/8558823
7. Araki E, Kawaguchi K, Kaneko S, Kaneda Y Design of deep ocean submarine cable observation network for earthquakes and tsunamis. In OCEANS 2008-MTS/IEEE Kobe Techno-Oceans 1–4 (IEEE, 2008); https://ieeexplore.ieee.org/document/4531071
8. Sauser B (2011) The Reliability of Tsunami Detection Buoys. In *MIT Technology Review, ed. Cambridge, MA*
9. Percival DB, Denbo DW, Gica E, Huang PY, Mofjeld HO, Spillane MC, Titov VV (2016) Evaluating Effectiveness of DART Buoy Networks. *arXiv preprint arXiv:1607.02795*

10. Sladen A, Rivet D, Ampuero JP, De Barros L, Hello Y, Calbris G, Lamare P (2019) Distributed sensing of earthquakes and ocean-solid Earth interactions on seafloor telecom cables. Nat Commun 10(1):5777
11. Williams EF, Fernández-Ruiz MR, Magalhaes R, Vanthillo R, Zhan Z, González-Herráez M, Martins HF (2019) Distributed sensing of microseisms and teleseisms with submarine dark fibers. Nat Commun 10(1):5778
12. Lindsey NJ, Dawe TC, Ajo-Franklin JB (2019) Illuminating seafloor faults and ocean dynamics with dark fiber distributed acoustic sensing. Science 366(6469):1103–1107
13. Becerril, C., Sladen, A., Ampuero, J. P., Preciado-Garbayo, J., Gonzalez-Herraez,M., Kutschera, F., … Bouchette, F. (2026). Towards Tsunami Early-Warning with Distributed Acoustic Sensing: Expected Seafloor Strains Induced by Tsunamis: C. Becerril et al.Pure and Applied Geophysics, 1–25
14. Zhan Z (2020) Distributed acoustic sensing turns fiber-optic cables into sensitive seismic antennas
15. Xiao H, Spica ZJ, Li J, Zhan Z (2024) Detection of earthquake infragravity and tsunami waves with underwater distributed acoustic sensing. Geophysical Research Letters, 51(2), e2023GL106767. https://doi.org/10.1029/2023GL106767
16. Tonegawa T, Araki E (2026) Observing broadband tsunamis in deep water via distributed acoustic sensing. Geophys Res Lett, 53(7), e2025GL120114.
17. Mazur, M., Fontaine, N. K., Ryf, R., Karrenbach, M., McLaughlin, K. L., Sperry, B.J., … Neilson, D. T. (2025, September). Submarine Cable Deep-Ocean Observation of Mega-Thrust Earthquake and Tsunami with 44,000 100-m Spaced Sensors. In 2025 European Conference on Optical Communications (ECOC) (pp. 1–4). IEEE
18. Calving-driven fjord dynamics resolved by seafloor fibre sensing
19. Baillet, M., Rivet, D., Trabattoni, A., Chèze, J., Peix, F., Ambrois, D., … Barrientos,S. (2025). Automatic earthquake catalogs from a permanent DAS offshore network. Journal of Geophysical Research: Solid Earth, 130(10), e2025JB031565
20. Rivet D, Baillet M, Trabattoni A, Van Den Ende M, Chèze J, Maron C, Sanchez R, Barrientos S, Epos-France (2025) Three underwater fiber-optic cables offshore of central Chile [Data set]. Epos-France Seismological Data Center. https://doi.org/10.15778/RESIF.F1
21. Lior, I., Rivet, D., Ampuero, J. P., Sladen, A., Barrientos, S., Sánchez-Olavarría,R., … Bustamante Prado, J. A. (2023). Magnitude estimation and ground motion prediction to harness fiber optic distributed acoustic sensing for earthquake early warning.*Scientific Reports*, *13*(1), 424
22. Strumia C, Trabattoni A, Scala A, Rivet D, Festa G (2026) Harnessing converted phases for rapid magnitude estimation and early warning with distributed acoustic sensing offshore Chile. Communications Earth & Environment
23. Williams, E. F., Ugalde, A., Martins, H. F., Becerril, C. E., Callies, J., Claret,M., … Zhan, Z. (2023). Fiber-optic observations of internal waves and tides. *Journal of Geophysical Research: Oceans*, *128*(9), e2023JC019980

24. Meulé, S., Pelaez-Quiñones, J., Bouchette, F., Sladen, A., Ponte, A., Maier, A.,… Coyle, P. (2024). Reconstruction of nearshore surface gravity wave heights from distributed acoustic sensing data. *Earth and Space Science*, *11*(11), e2024EA003589
25. Glover HE, Wengrove ME, Holman R (2024) Measuring hydrodynamics and exploring nearshore processes using distributed sensing of fiber-optic cable strain. Coast Eng 190:104487
26. Kohler MD, Bowden DC, Ampuero JP, Shi J (2020) Globally scattered 2011 Tohoku tsunami waves from a seafloor sensor array in the Northeast Pacific ocean. Journal of Geophysical Research: Solid Earth, 125(11), e2020JB020221
27. Trabattoni A, Baillet M, van den Ende M, Rivet D, Stutzmann E, Strumia C, Biagioli F (2025) Xdas: A python framework for distributed acoustic sensing. Seismological Research Letters
28. Babeyko A (2012) EasyWave: Fast Tsunami Simulation Tool for Early Warning. GFZ German Research Centre for Geosciences, Potsdam
29. Watada S, Kusumoto S, Satake K (2014) Traveltime delay and initial phase reversal of distant tsunamis coupled with the self-gravitating elastic earth. J Geophys Research: Solid Earth 119(5):4287–4310
30. National Geophysical Data Center (2006) 2-minute Gridded Global Relief Data (ETOPO2v2). National Geophysical Data Center, NOAA
31. Liu PL-F, Woo S-B, Cho Y-S (1998) Computer programs for tsunami propagation and inundation. Cornell University
32. An C, Sepúlveda I, Liu PL-F (2014) Tsunami source and its validation of the 2014 Iquique, Chile, earthquake. Geophys Res Lett 41(11):3988–3994. https://doi.org/10.1002/2014gl060567
33. GEBCO Compilation Group (2024) GEBCO 2024 Grid. https://doi.org/10.5285/1c44ce99-0a0d-5f4f-e063-7086abc0ea0f
34. Ayumu Mizutani T, Saito (2026) Tsunami-induced crustal strain: analytical solutions for tsunami observation using fiber optic sensing. Geophys J Int ggag391. https://doi.org/10.1093/gji/ggag391

# Figures

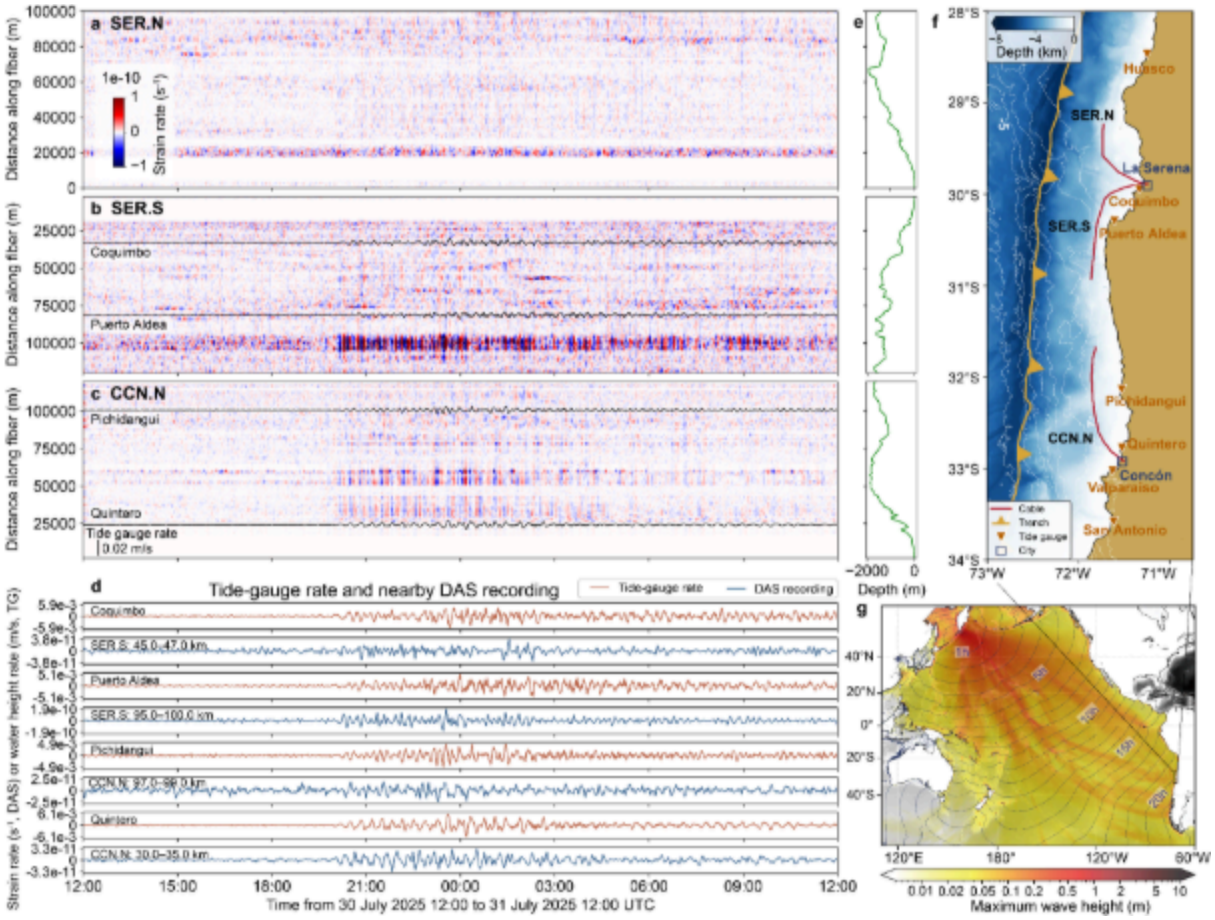
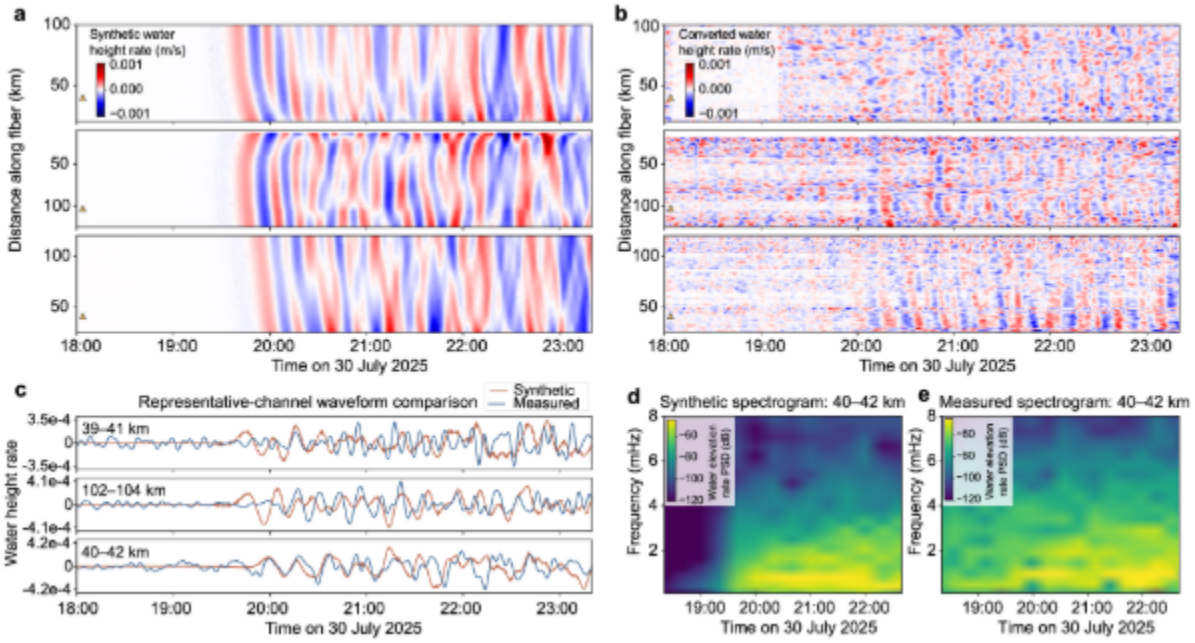


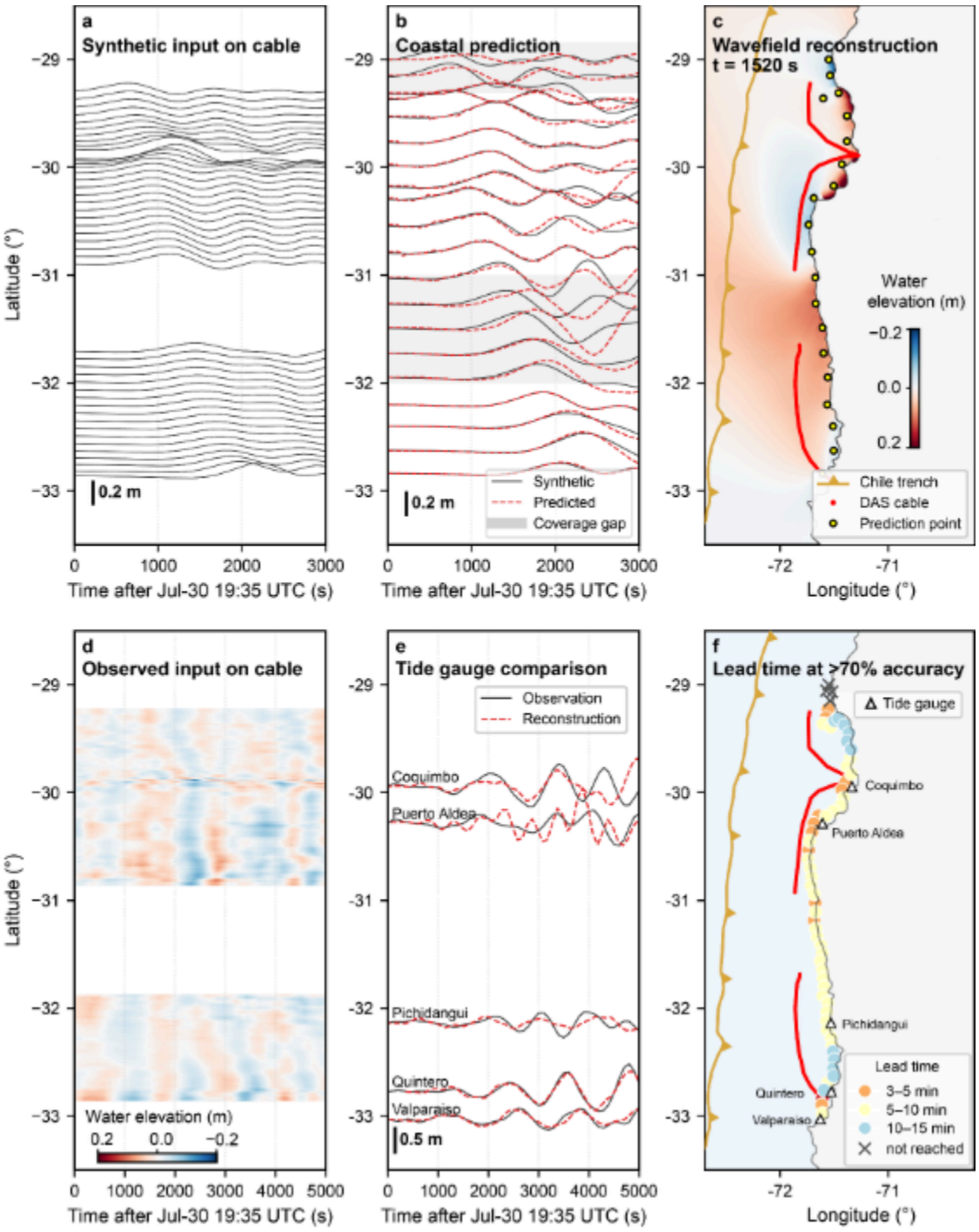

**Figure 1**

**Offshore DAS observations of the 2025 Kamchatka tsunami along submarine telecommunication cable off Chile. a-c**, Processed DAS strain-rate records from the SER.N, SER.S and CCN.N cable segments. Channels on each segment are ordered from north to south, from the top to the bottom of each panel. The vertical axis denotes optical distance along the fibre from the interrogator. Zero-valued bands indicate muted noisy channels or data gaps and are not interpreted as physical zero-amplitude observations. Black traces show tide-gauge records projected onto the nearest cable locations after demeaning and band-pass filtering between 300 and 2,000 s. **d**, Comparison between tide-gauge-rate waveforms and median DAS recordings from representative nearby cable segments selected to avoid strong noise contamination, showing consistent tsunami arrivals around 20:00 UTC and similar dominant periods in coastal and offshore records. **e**, Seafloor depth along each fibre. **f**, Map of the study region showing cable routes, the subduction trench, tide-gauge stations and coastal cities. **g**, Relative locations of the earthquake source and DAS array, modelled maximum tsunami wave height across the Pacific, and tsunami travel-time contours.




## Figure 2

**Comparison of simulated and DAS-derived propagating tsunami wavefields. a**, Synthetic tsunami water-height-rate signals along the SER.N, SER.S and CCN.N cable segments, shown from top to bottom. **b**, Corresponding DAS-derived water elevation rate converted from strain rate using channel-wise empirical coefficients, estimated from the RMS of the synthetic waveforms over the tsunami window from 20:00 UTC on 30 July to 00:00 UTC on 31 July 2025. Yellow triangles mark the channels used for waveform comparison in **c**. **c**, Waveform comparisons between simulated and DAS-derived water-height rate for selected cable sections. **d**,**e**, Spectrograms of the simulated and DAS-derived signals, respectively, for the 40-42 km window on CCN.N, showing similar dominant tsunami-period energy and comparable frequency dispersion through time.




## Figure 3

**Wavefield reconstruction from synthetic and observed cable records. a**, Synthetic cable water-elevation waveforms used as input to the reconstruction benchmark, plotted over time and vertically offset by latitude. **b**, Synthetic coastal water elevation (black) and corresponding reconstruction prediction (red dashed) at the coastal validation points shown in **c**; grey bands mark gaps in effective wavefield sampling by the cable array.. **c**, Reconstructed water-elevation field using all synthetic cable waveforms available by 1,520 s after 19:35 UTC on 30 July. Yellow circles mark coastal prediction points. **d**, DAS-observation-derived cable input after empirical amplitude calibration and temporal integration. Channels with water-elevation RMS <0.01 m were assigned zero reconstruction weight and are not plotted. **e**, Tide-

gauge water elevation (black) and observation-based reconstruction (red dashed) at five coastal tide gauges. Tide-gauge records are filtered following the DAS preprocessing workflow (zero-phase 300-2,000 s), and reconstructed traces are shifted by the station-wise lag that maximizes cross-correlation over 0-4,000 s; shifts are <150 s except at Quintero (347 s), where unresolved nearshore propagation may explain the larger offset (Fig. S6; unshifted comparison in Fig. S7). **f**, Synthetic-benchmark lead time for coastal first-peak prediction. Lead time is defined as the interval between the earliest update at which the first-peak amplitude at a validation site is predicted with <30% relative error and the arrival of that peak at the same site. Coloured circles show lead times at validation points near the 100 m isobath; these lead times are conservative estimates because they exclude the additional propagation time to the coastline, estimated separately in Fig. S5. Forecasts are progressively updated as more cable data becomes available. Triangles mark the five tide gauges used in **e**.

## Supplementary Files

This is a list of supplementary files associated with this preprint. Click to download.

- Supplementaryinformation.docx